Journal of Microscopy, Vol. 224, Pt 3 December 2006, pp. 213–232
Received 13 April 2006; accepted 28 June 2006

TUTORIAL REVIEW

A guided tour into subcellular colocalization analysis in light microscopy

S. BOLTE* & F. P. CORDELIÈRES†
**Plateforme d'Imagerie et de Biologie Cellulaire, IFR 87 'la Plante et son Environnement', Institut des Sciences du Végétal, Avenue de la Terrasse, 91198 Gif-sur-Yvette Cedex, France*
†Institut Curie, CNRS UMR 146, Plateforme d'Imagerie Cellulaire et Tissulaire, Bâtiment 112, Centre Universitaire, 91405 Orsay Cedex, France

Key words. Colocalization, confocal microscopy, fluorescence microscopy, image analysis, wide-field microscopy.

Summary

It is generally accepted that the functional compartmentalization of eukaryotic cells is reflected by the differential occurrence of proteins in their compartments. The location and physiological function of a protein are closely related; local information of a protein is thus crucial to understanding its role in biological processes. The visualization of proteins residing on intracellular structures by fluorescence microscopy has become a routine approach in cell biology and is increasingly used to assess their colocalization with well-characterized markers. However, image-analysis methods for colocalization studies are a field of contention and enigma. We have therefore undertaken to review the most currently used colocalization analysis methods, introducing the basic optical concepts important for image acquisition and subsequent analysis. We provide a summary of practical tips for image acquisition and treatment that should precede proper colocalization analysis. Furthermore, we discuss the application and feasibility of colocalization tools for various biological colocalization situations and discuss their respective strengths and weaknesses. We have created a novel toolbox for subcellular colocalization analysis under ImageJ, named JACoP, that integrates current global statistic methods and a novel object-based approach.

Introduction

Colocalization analysis in optical microscopy is an issue that is afflicted with ambiguity and inconsistency. Cell biologists have to choose between a rather simplistic qualitative evaluation of overlapping pixels and a bulk of fairly complex solutions, most of them based on global statistic analysis of pixel intensity distributions (Manders *et al.*, 2003; Costes *et al.*, 2004; Li *et al.*, 2004). The complexity of some of these different analysis tools makes it difficult to implement the appropriate method and reflects the fact that the majority of colocalization situations demand customized approaches. All-round analysis tools do not necessarily fit all circumstances as cells contain a plethora of structures of multiple morphologies, starting from linear elements of the cytoskeleton, punctate and isotropic compartments such as vesicles, endosomes or vacuoles, going to more complex anisotropic forms such as Golgi stacks and the network-like endoplasmic reticulum. The colocalization of two or more markers within these cellular structures may be defined as an overlap in the physical distribution of the molecular populations within a three-dimensional volume, where this may be complete or partial overlap.

The limits of resolution in optical microscopy imply an uncertainty of the physical dimensions and location of small objects in the two-dimensional and even more in the three-dimensional space. The frequent question is: are two fluorochromes located on the same physical structure or on two distinct structures in a three-dimensional volume? The answer depends on the definition of terms and limits, bearing in mind that the fluorochrome distribution may be in the nanometre range whereas the optical microscope's resolution is closer to the micrometre. The veracity of any statement concerning colocalization will thus be limited not only by a good understanding of the three-dimensional organization of the cell and its subcellular compartments, the quality and reliability of the labelling techniques or the faithfulness of the markers applied to highlight and identify the different cellular addresses. It will be equally limited by the dimensions defined by the optical system and the image-acquisition procedure. The authentic

Correspondence to: S. Bolte. Tel: 0033 69863130; Fax: 0033 169 86 1703;
e-mail: Susanne.Bolte@isv.cnrs-gif.fr.
F. P. Cordelières. E-mail: Fabrice.Cordelieres@curie.u-psud.fr

visualization of this three-dimensional organization thus depends on a good control of the optical system used and, as a matter of fact, on the mastery of some basics in optics, image processing and analysis.

We therefore propose a guideline for the acquisition, qualitative evaluation and quantification of data used for colocalization purposes. We give an overview on the state of the art of colocalization analysis by reviewing the most important features available in standard imaging software. Finally, we introduce a novel tool for colocalization analysis, named JACoP (Just Another Co-localization Plugin), that combines these currently used colocalization methods and an object-based tool named three-dimensional object counter as plugins to the public domain Image J software (Rasband, 1997–2006).

Before getting started

Basic optical principles

Before using any microscope to collect images, one has to be aware of its limitations. One of these is closely linked to the dual nature of light, which is both a wave and particle phenomenon. The objective lens allows the collection of light that is only partial and is quantified by a parameter called numerical aperture (NA). It is linked to the angle of collection of light emitted from the specimen and will determine the ability to distinguish between two adjacent punctate light sources. Under critical illumination, the NA of the condenser illuminating the sample should be the same as that of the objective. In epifluorescence microscopy, the objective acts as the condenser and so this critical condition is met. Each point of a light wave exiting a lens can then be considered as a single light source emitting a circular wave front (Huygens' principle). Therefore, when placing a screen after a lens, a diffraction pattern can be collected, resulting from interferences between adjacent waves. This pattern defines the two-dimensional diffraction figure, which consists of concentric rings alternating from light to dark (Fig. 1A). The first light disc is called the Airy disc (Inoué, 1995). When tracing a line through this pattern, we obtain a curve (Fig. 1D) representing the fluorescence intensity distribution of the particle along this line. The Airy disc then corresponds to the area below the major peak of this curve and the full width at half maximum of this fluorescence intensity curve (Fig. 1D) is used to define the resolution of the optical system.

To be able to distinguish between two similar punctate light sources through a lens, the corresponding Airy discs should

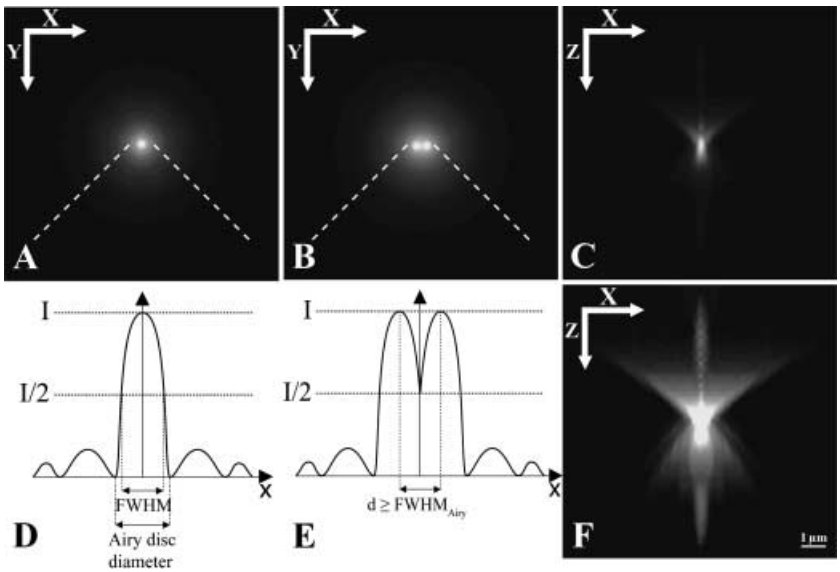

Fig. 1. An image of a point is not a point but a pattern of diffracted light. (A–C) Two-dimensional diffraction patterns of the centres of 170-nm green fluorescent beads seen through a wide-field microscope. (D) and (E) Corresponding fluorescence intensity curves traced along a line passing through the centre of the beads in (A) and (B), respectively (I being the maximum intensity). (F) Three-dimensional projection of the z-stack representing the diffraction pattern of the fluorescent bead seen from the side. (A) and (D) Note the concentric light rings around the Airy disc of a single fluorescent bead. The Airy disc is the first light patch in this diffraction pattern. Two characteristic dimensions may describe the bell-shaped curve: 1, Airy disc diameter, which is the distance between the two points where the first light ring extinguishes; 2, full width at half maximum (FWHM), which is directly related to resolution (see below). (B) and (E) Diffraction pattern of two beads. Two objects are resolved if their corresponding intensity curves at I/2 are distinct. The critical distance d between the centres of the intensity curves defines the lateral resolution (x, y) of the optical system. It is equal to FWHM. (C) Three-dimensional projection of a z-series of a fluorescent bead seen from the side (x, z) representing the diffraction pattern of the same fluorescent bead. Note that the axial resolution (z) of an optical system is not as good as the lateral resolution (x, y). (F) The diffraction pattern is not symmetric around the focal plane, being more pronounced on the upper side proximal to the objective. Note that a bright 10-nm bead would produce patterns of the same dimensions as this 170-nm bead.

Table 1. The laws of Abbe and their effect on optical resolution and pixel sizes in wide-field and confocal microscopy.

	Wide-field		Confocal	
	Lateral resolution dx, y	Axial resolution dx, z	Lateral resolution dx, y	Axial resolution dx, z
Expression	$0.61\,\lambda_{em}/NA$	$2\,\lambda_{em}/NA^2$	$0.4\,\lambda_{em}/NA$	$1.4\,\lambda_{em}/NA^2$
Limit resolution of a 63× oil immersion objective with NA = 1.32 at λ_{em} = 500 nm	232 nm	574 nm	152 nm	402 nm
Minimal justified pixel size for this objective	101 nm	250 nm	66 nm	175 nm

NA, numerical aperture.

be apart from each other (Fig. 1B). The minimal distance (d) between their centres, which gives an integral energy distribution whose minimum is $I/2$, is taken to define the optical resolution or separating power (Fig. 1E). This parameter may be calculated according to the laws of Abbe (Table 1). It depends on the NA of the objective that, in turn, is dependent on the refractive index of the medium and on the wavelength of emitted light. Furthermore, the optical resolution depends on the type of microscope used. A wide-field microscope may separate two dots 200 nm apart from each other (63× oil immersion objective, NA = 1.32, emission wavelength 510 nm). Introducing a confocal pinhole of 1 Airy width (i.e. an aperture whose diameter corresponds to the diameter of the first Airy disc for the current wavelength) into the optical system will result in an improvement by approximately 30% of this lateral resolution because out-of-focus light is eliminated from the detector (Abbe, 1873, 1874; Minksy, 1961). As a first approximation, only light coming from the first Airy disc is collected. This means that the aperture of the pinhole will mainly depend on the objective used and on the refraction indexes of all media encountered by light on its way to and away from the sample. It should be set to 1 Airy unit to ensure confocal acquisition.

Biological samples are not two-dimensional limited. The use of stepper motors or piezo-electrical devices in wide-field or confocal laser scanning microscopes allows the collection of optical sections representing the three-dimensional volume of the sample by moving the objective relative to the object or vice versa. As a consequence, the diffraction pattern of light should be considered as three-dimensional information and will define the point spread function (PSF) (Castelman, 1979). The Airy disc along the z-axis appears elongated, like a rugby ball (Fig. 1C), and the overall diffraction pattern of light has axial symmetry along the z-axis with a three-dimensional shape of the PSF that is hourglass-like (Fig. 1F). The minimum distance separating two distinguishable adjacent Airy discs along the depth of the PSF will define the axial resolution of the microscope (Table 1). The optical laws introduced here imply that colocalization must be measured in the three-dimensional space. The imbalance between the lateral and axial resolution of optical microscopes leads to a distortion of a round-shaped object along the z-axis. Bear in mind that a brilliant nanometric object will nevertheless yield an image whose waist is at least 200 nm and whose depth is about 500 nm, as defined by the Airy disc. Therefore, any colocalization analysis must be carried out in the three-dimensional space. Furthermore, it is self-evident that three-dimensional projections of image stacks must not be analysed as they shrink volumetric information to two dimensions, leaving aside the depth component.

Digital imaging

The limits of optical resolution depend on the PSF and directly influence imaging parameters. Once an image has been formed by the optical system, it will be collected by an electronic device that will translate a light signal into an electronic signal for further processing by the computer. Microscope images are generally captured either by digital cameras (a parallel matrix) or photomultipliers (a sweep of point measurements) that compose the final image as a matrix of discrete picture elements (pixels). The definition of an image as pixels implies some precautions in image acquisition. To resolve two points and to avoid under- or over-sampling, the pixel size applied should be equal to the lateral limit of resolution between the two points divided by at least 2 according to the Nyquist sampling theorem (Oppenheim *et al.*, 1983). In microscopy it is widely accepted that, according to this theorem, to reproduce faithfully formed images the detector should collect light at 2.3× the frequency of the original signal. Basically, this means that the projected image of a single dot should appear on at least two adjacent sensitive areas of the detector in a given axis, namely on four pixels (2 × 2 for x, y). Therefore, the sampling frequency should be at least twice greater than the resolution of the current dimension (x, y or z). For two-dimensional acquisitions this means that the minimal justified pixel size is calculated by dividing the lateral resolution by at least 2. In three-dimensional imaging, the size of the z-step relies on the same laws, i.e. the axial resolution also has to be divided at least by 2. The minimal justified pixel size and the z-step size depend on the NA of the objective, e.g. a 63×

objective (oil immersion, NA = 1.32) collecting emitted light of 500 nm with a lateral resolution of 232 nm and an axial resolution of 574 nm implies a minimal justified pixel size of 101 nm and a z-step size of 250 nm (see also Table 1).

It is important to note that image acquisition for colocalization analysis should always be carried out on several subsequent optical sections, i.e. in three dimensions, and near to the resolution limit of the optical system, i.e. with the appropriate justified pixel size and z-step size.

A frequent mistake in microscopy is oversampling. This happens when a single subresolution light source is fitted on more than 2 (or 2.3) adjacent pixels on the detector, i.e. using pixel sizes smaller that the minimal justified pixel size defined by optical resolution and the Nyquist theorem. The resulting image looks larger but the signal looks dimmer as the light is spread out on more parts of the detector than required. Even though the sample seems to be highly magnified, there is no gain in resolution as the optical resolution limit cannot be surmounted. It is furthermore important to avoid saturation of images, as saturated pixels may not be quantified properly because information of the most intense grey level values in a histogram gets lost. It is difficult to judge by eye if an image composed of grey values, or green or red hues is saturated, as the human eye is not sensitive enough. Our eye can, however, distinguish between hundreds of colours and therefore most image-acquisition software provides colour look-up tables with hues indicating saturated pixels and providing the possibility of adjusting the dynamics of grey values on the detector side.

Choice of the acquisition technique

We have learned that optimal image acquisition for colocalization analysis relies mainly on the limits of optical resolution; it is thus important to adapt the optical system to the biological question and to choose the appropriate microscope. Confocal imaging gives high resolution, eliminating out-of-focus light by introducing a pinhole on the detector side. Confocal imaging is recommended when handling thick or highly diffusive samples such as plant tissue or brain tissue. It is important to note that image acquisition with standard confocal microscopes is fairly slow (1 s image^{-1}) and thus has been more suited to three-dimensional imaging of colocalization in fixed samples rather than in live samples. A disadvantage of excluding out-of-focus light from the detector by a confocal pinhole is that valuable information may get lost and low signals might not be detected (Fig. 2A). The Airy disc in fact comprises only 10% of the total energy from a point source. Wide-field microscopes equipped with rapid charge-coupled devices might be a good alternative if one wants to cope with these kinds of problems, as three-dimensional acquisition can be performed very rapidly (20 ms image^{-1}) and low-intensity information will not be lost, as all information will be collected by the detector. The advantage of collecting all information, i.e. out-of-focus light, is a constraint at the same time as images are blurred and difficult to analyse directly (Fig. 2B). This out-of focus light interferes with accurate colocalization analysis and makes image restoration necessary. The image that is formed on a detector by a single particle (with a size below optical resolution) will be defined by the PSF of the optical system used. Optics convolute image information. This means that the hourglass-like shape of the PSF is a model for the three-dimensional spread of light caused by the optical system. Reassigning the out-of-focus blurred light to its origin is performed by a process called deconvolution (Fig. 2C). This is a computational technique that includes methods that help to reattribute the signal spread in three dimensions according to the PSF to its origin. Deconvolution may restore the resolution of images in both wide-field and confocal microscopy and is the subject of some excellent reviews (Wallace & Swedlow, 2001; Sibarita, 2005). Deconvolution in combination with wide-field microscopy is restricted to thin objects (< 50 μm). Although giving a more resolved image, one of the major pitfalls of deconvolution techniques arises from the complexity of the image. An image must be considered as a composition of multiple PSFs because

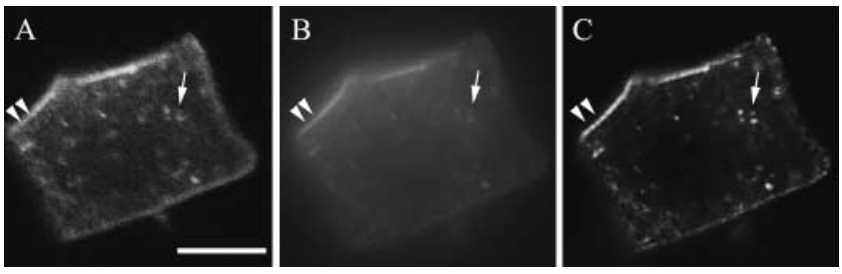

Fig. 2. Comparison of cellular imaging by confocal and wide-field microscopy. Median plane of a maize root cell immunolabelled with AtPIN1/Cyanine3.18 (Boutté *et al.*, 2006). Scale bar, 10 μm. Images were acquired by confocal (A) and wide-field (B) and wide-field followed by deconvolution (C) microscopy. All images show polar distribution of At-PIN1 on the plasma membrane and on subcellular punctiform structures. Note that the raw single confocal image (A) is sharp because out-of-focus light was cut off by the pinhole. The wide-field image (B) is typically blurred. (C) Deconvolution of the wide-field image has reassigned the out-of-focus light to its origin, with a gain in sharpness and contrast. Deconvolution has led to a slight gain of information compared with confocal microscopy; low-intensity signals that were not detected by confocal microscopy have become visible after deconvolution of the wide-field data (arrows). Protein subdomains at the plasma membrane may also be refined by deconvolution of wide-field images (arrowheads).

each fluorescent signal of the sample results in a diffraction pattern that is displayed on the detector. Moreover, PSFs are not constant in the three-dimensional volume imaged, as the PSFs are degraded in the depth of the sample and appear to be disturbed at the interface of two media with different refraction indexes.

Further techniques have been developed that overcome the constraints of acquisition rate or out-of-focus light. These include structured illumination and rapid confocal devices and are discussed in detail elsewhere (Brown *et al.*, 2006; Garini *et al.*, 2005). In this work, however, we will focus on commonly available standard confocal and wide-field microscopy.

Incidence of fluorochromes, light sources, filters and objectives

It has already been mentioned that the resolution capacity of an optical system depends on the angular properties of its objective, the composite refractive index of all media crossed by light and the emission wavelength of the fluorochromes used (Table 1). A number of fluorochromes may be used to label different proteins of interest. The ability to distinguish between individual emission spectra is a primary concern, reinforced by selective excitation of only one fluorochrome at a time. This aim is achieved by optimizing: (i) the choice of fluorochromes, (ii) the selectivity of excitation and (iii) the means of emission discrimination.

Any fluorescent reagent can be characterized by its excitation and emission spectra, which in turn may depend upon the fluorophore's environment (Valeur, 2002). These classical curves, respectively, represent the probability of making an electronic transition from ground to excited state when exposed to photon energy of a particular wavelength and to release a photon at a particular wavelength when fulfilling the opposite transition. The first value to be taken into account is the Stoke's shift, which is defined as the spectrum distance between the most efficient excitation (peak in the excitation spectra) and the maximum of emission. The ability to sort emission from excitation light depends partly on this value, as incident light is about 10^4 more intense than the signal being recovered (Tsien & Waggoner, 1995). The width of excitation and emission curves contributes to the practicality of fluorescent reagents for distinctiveness; the narrower the curves, the easier the fluorochromes will be to separate. However, this is only true for fluorochrome pairs with spectra far enough apart from each other.

A wide range of fluorescent reagents is now available to cover the spectrum from visible to near infrared. Fluorochromes may be coupled to primary or secondary antibodies for immunolabelling. Other fluorescent compounds may accumulate in specific cellular compartments, such as nuclei, endoplasmic reticulum, Golgi apparatus, vacuoles, endosomes, mitochondria or peroxisomes. Genetically encoded targeted fluorescent proteins from jellyfish or corals are readily available and are helpful in live cell studies. Newly engineered semiconductor colloidal particles (Q-Dots) are adapted for single molecule labelling (Dahan *et al.*, 2003; Gao *et al.*, 2004).

When choosing fluorochrome combinations for colocalization studies, their spectra must be unambiguously distinctive. Furthermore, it has to be considered that these spectra may be dependent on the physical environment (Bolte *et al.*, 2004a, 2006).

We have to introduce here the terms bleed-through and cross-talk of fluorochromes, as avoiding these phenomena is crucial to colocalization analysis. Bleed-through is the passage of fluorescence emission in an inappropriate detection channel caused by an overlap of emission spectra (Fig. 3). Cross-talk is given when several fluorochromes are excited with the same wavelength at a time because their excitation spectra partially overlap.

Let's consider the fluorochrome couple fluorescein isothiocyanate (FITC) and Cyanine3.18 (Cy3), which is frequently used for immunolabelling for colocalization analysis (Fig. 3). The excitation spectra of these two fluorochromes seem to be well apart with FITC peaking at 494 nm and Cy3 with a minor excitation peak at 514 nm and a major excitation peak at 554 nm. Even using the narrow laser line of 488 nm for FITC excitation, one may already observe a slight cross-talk between FITC and Cy3, as Cy3 excitation spectra have slight but significant

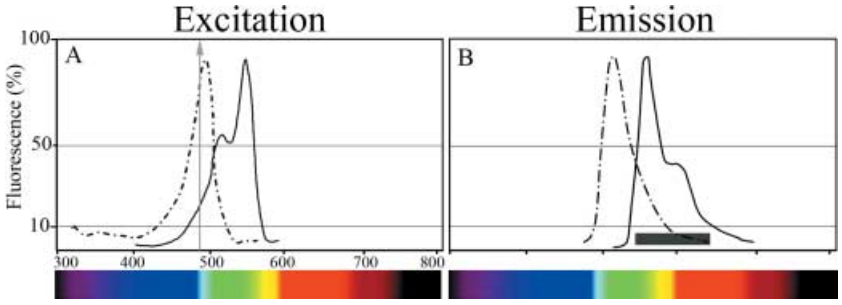

Fig. 3. Definition of cross-talk and bleed-through with the fluorochrome couple fluorescein iso-thiocyanate/Cyanine3.18 (FITC/Cy3). (A) Excitation spectra of FITC (broken line, max. 490 nm) and Cy3 (solid line, max. 552 nm). The grey arrow marks the position of the standard 488-nm laser line of confocal microscopes. Note the overlap of the excitation spectra at 488 nm (cross-talk). (B) Emission spectra of FITC (broken line, max. 520 nm) and Cy3 (solid line, max. 570 nm). The grey bar marks the typical detection window of Cy3. Note the overlap of FITC and Cy3 emission in this detection window (bleed-through).

absorbance at 488 nm (Fig. 3A). Moreover, even when exciting FITC and Cy3 sequentially with 488 and 543 nm, one may detect a bleed-through of the lower energy (yellow) part of the FITC emission coinciding with the emission maximum of Cy3 in the Cy3 detection channel (Fig. 3B). When using band-pass-filtered excitation light, such as in wide-field microscopy, instead of laser lines or monochromatic light, the situation may get worse. It is thus essential to apply some simple strategies that help to avoid cross-talk and bleed-through. Firstly, it is always important to have single labelled controls for each fluorochrome used. In this way one may check for bleed-through between fluorochromes on the detector side. Secondly, in laser scanning microscopy, it is highly recommended to perform sequential acquisitions exciting one fluorochrome at a time and switching between the detectors concomitantly.

Another method of meeting the challenge is spectral unmixing, a quite simple mathematical operation that was originally developed for satellite imaging. Spectral unmixing software packages are often included in image-acquisition software of the microscope manufacturers. By this technique, which is a correction of spectral bleed-through, it is also possible to enhance the chromatic resolution of fluorescence microscopy. Two general approaches may be distinguished. One is to perform microspectrofluorometry and to use the model (or measure) of separate fluorochromes to perform spectral deconvolution of the complex raw image (Zimmermann *et al.*, 2003). This implies curve fitting and extrapolation. A second, simpler approach is to experimentally determine the bleed-through factor for a given optical configuration and to use this to derive corrected values for each pixel. This is analogous to pulse compensation in flow cytometry.

To unmix the spectra of fluorochromes with strongly overlapping emission spectra, it is necessary to assign the contribution of different fluorochromes to the overall signal. This is done first by determining the spectral properties of the individual fluorochromes under the same imaging conditions used for the multilabelled samples.

We will again consider the two fluorochromes FITC and Cy3 seen through their respective filters A and B. Using a mono-labelled slide, FITC seen through A will give an intensity a_{FITC} and b_{FITC} through B. Analogous notations will be used for Cy3. Then imaging a dual-labelled FITC and Cy3 sample, the image through A will be $a_{FITC} + a_{Cy3}$; the image of FITC acquired using the appropriate filter is contaminated by a contribution from Cy3. The same phenomenon will occur for the image of Cy3 collected through B ($b_{FITC} + b_{Cy3}$). The use of mono-labelled slides allows the estimation of the relative contribution of FITC to the image of Cy3 and is used to give a more reliable image of FITC ($a_{FITC} + b_{FITC}$) and Cy3 ($a_{Cy3} + b_{Cy3}$). The ratio FITC : Cy3 of the average intensities of single fluorochrome-labelled structures measured at the two excitation wavelengths for FITC and Cy3, respectively, gives a constant that is specific for each fluorochrome under given experimental conditions and fixed settings. The intensity is then redistributed in order to restore a corrected signal for each colour channel undisturbed by emission from the other fluorochrome.

Fluorochromes may also transfer energy to each other by Förster resonance energy transfer (for review see Jares-Erijman & Jovin, 2003). This non-radiative energy transfer may occur when the emission spectrum of the first fluorochrome (donor) overlaps with the excitation spectrum of the second fluorochrome (acceptor) and if the donor and acceptor molecules are in close vicinity (10–100 Å). Förster resonance energy transfer causes a reduction of the emission of the donor fluorochrome and an increase of the emission of the acceptor fluorochrome, therefore resulting in a misbalanced intensity ratio between the two image channels. It is thus also crucial to select the first fluorochrome with an emission spectrum as distinct as possible from the excitation spectrum of the second fluorochrome in order to avoid Förster resonance energy transfer effects that would complicate the interpretation of colocalization data.

The choice of light sources and appropriate filters is the next step for appropriate discrimination between fluorescence spectra. We have already learned that using monochromatic light from a laser source in a confocal microscope lowers the risk of exciting several fluorochromes at a time, even if it does not exclude cross-talk. In wide-field microscopy mercury or xenon lamps have spectral output spanning from UV to infrared, with numerous peaked bands, notably in the case of mercury. They are used in combination with appropriate filters or as part of monochromators. As a consequence, when using filtered light the excitation is not monochromatic and the risk of exciting several fluorochromes at a time is high. This inconvenience may be partially circumvented by using a monochromator to generate a suitably narrow subrange of wavelengths that may be optimized for each situation. However, care has to be taken as the monochromator may generate a slight excitation leakage on both boundaries of the narrowed excitation window, leading to possible cross-talk.

The choice of objectives used for colocalization analysis at the subcellular level is crucial to attain optimal resolution. Objectives used should be of high quality, with a high NA (> 1.3) and magnifications adapted to the camera in wide-field microscopy. In both kinds of microscopy, the NA is critical, as z-resolution improves as a function of $(NA)^2$ (see Table 1). Objectives should be corrected for chromatic and spherical aberrations. Chromatic aberrations are due to the failure of the lens to bring light of different wavelengths to a common focus. Spherical aberrations come from the failure of a lens system to image the central and peripheral rays at the same focal plane. Objectives corrected for both aberrations are called plan-apochromatic and confocal microscopes are usually equipped with these. For colocalization analyses it is recommended to use immersion objectives to reduce aberrations due to the refraction index changes. This means oil immersion for fixed mounted specimens and aqueous immersion for live cell studies.

Checking the system

Before performing colocalization measurements, it is important to check the microscope's integrity. This may be done by measuring the PSF of the optical system (Scalettar *et al*., 1996; Wallace & Swedlow, 2001), using objects whose sizes are just matching or below the microscope's resolution. Small fluorochrome-labelled polystyrene beads of 100–170 nm are available for this. Remember that the resolution of the optical system is closely linked to the NA of the objective used, refraction index of the mounting medium, immersion medium (oil, glycerol or water), coverslip thickness and emission wavelength of the fluorochrome. Individual PSFs should thus be measured on fluorescent beads of the respective wavelengths mounted in identical conditions to the sample and with the objectives that are used for colocalization analysis.

The shape of the PSF of a fluorescent bead gives an intuitive characterization of the image quality. It can also be used to test the objective performance and integrity. A dirty objective or a non-homogeneous immersion medium will result in a deformed PSF (Sibarita, 2005). Returning to objective quality, one may be surprised to observe that the maxima of intensity for all fluorochromes may not be coincident in space. This observation is due to an imperfection in the lens design or manufacture resulting in a variable focalization of light as a function of wavelength. Even if most manufactured objectives are apochromatic, the refraction index of immersion oil is dependent on both temperature and wavelength, giving rise to this phenomenon. Likewise, glycerol is hygroscopic and its refractive index will in practice change with time. As a consequence, and especially in the case of colocalization studies, the chromatic aberration may in this case be determined and the shift between images corrected (Manders, 1997).

Pre-processing of images

As perfect as an optical system can be, we have already seen that an image is an imperfect representation of the biological system. The illumination system used in wide-field microscopy will impair the image, especially if it is not well aligned. As a consequence, the field of view may not be illuminated in a homogeneous fashion. When trying to quantify colocalization as a coincidence of intensity distributions, one may need to correct uneven illumination. This may simply be done by correcting the image of the sample using a bright image of an empty field. This correction is achieved by dividing the former image by the latter. This operation may be carried out with ImageJ using the Image Calculator function.

Noise is another major problem in digital imaging. However, before trying to correct images for it, we must first address its possible origins. Illumination systems such as mercury or xenon lamps are not continuously providing photons and may be considered as 'blinking' sources. As a consequence, even though all regions of a field will statistically be hit by the same number of photons over a long period, the number of photons exciting fluorochromes is not the same when comparing a region with its neighbours on a millisecond scale. Similarly, the emission of a photon by a fluorochrome is dependent on its probability of returning to ground state. This so-called photon noise will imprint a salt-and-pepper-like background on the image. As it is a stochastic function, it can be partially overcome by increasing the exposure time on charge-coupled device cameras or slowing the frequency (increasing dwell time) of scanning on a confocal microscope. One may also collect successive images and average them.

Furthermore, noise originating from the detection device (electronic noise or dark current) may be limited by cooling the detection devices.

Intrinsic statistical noise follows a Poisson distribution. To remove this kind of noise, images may be post-processed using adaptive filtering. This may be done by changing the pixel value to an intensity calculated on the basis of the local statistical properties of both the signal and noise of neighbouring pixels. This may, however, result in a loss of features such as sharp contours. Out-of-focus light may be reassigned to its origin by deconvolution as already mentioned (Wang, 1998).

Finally, imaging may be impaired by background coming from either natural fluorescence of the sample or being generated when preparing the sample. In most cases, nothing can be done after image acquisition unless a uniform background is observed. In this special case, its mean intensity is determined and this value is subtracted across the full image. More subtle processes exist, such as spectral unmixing, that may give better results on specific problems and the reader may consult appropriate image-processing handbooks (Gonzales & Woods, 1993; Pawley, 1995; Ronot & Usson, 2001).

Visualizing colocalization

When visualizing colocalization, the elementary method is to present results as a simple overlay composed of the different channels, each image being pseudo coloured using an appropriate colour look-up table. For example, it is commonly accepted that the dual-channel look-up table for green and red will give rise to yellow hotspots where the two molecules of interest are present in the same pixels. However, anyone who has been using this method knows its limits. The presence of yellow spots is highly dependent on the relative signal intensity collected in both channels; the overlay image will only give a reliable representation of colocalization in the precise case where both images exhibit similar grey level dynamics, i.e. when the histograms of each channel are similar. This is rarely the case when imaging two fluorochromes with differential signal strength. As a consequence, image processing is required to match the dynamics of one image to the other. This is often done by histogram stretching. However, histogram stretching may result in falsified observations because the resultant image does not reflect the true stoichiometry of the molecules

imaged. An alternative to histogram stretching is the use of specifically designed look-up tables that will enhance the visual effect of coincidental locations (Demandolx & Davoust, 1997). These authors proposed a new pseudo-colourization method in the form of a look-up table enabling visualization of the first fluorophore alone in cyan and the second alone in magenta. As the colocalization event is generally difficult to visualize and as the ratio of fluorophores may vary locally, they used green and red to highlight regions where one fluorophore is more intense than the other and yellow in the case where both intensities are the same. This method improved the discrimination of fluorescence ratios between FITC and Texas Red.

Measuring colocalization

Overlay methods help to generate visual estimates of colocalization events in two-dimensional images; however, they neither reflect the three-dimensional nature of the biological probe nor the restrained resolution along the z-axis. Furthermore, these overlay methods are not appropriate for quantification purposes because they may result in misinterpretation of relative proportions of molecules. To overcome these problems image analysis is crucial. There are two basic ways to evaluate colocalization events, a global statistic approach that performs intensity correlation coefficient-based (ICCB) analyses and an object-based approach.

The theory behind some of these tools is rather complex and sometimes difficult to compile and the results obtained have been difficult to compare until now. Here, we introduce a public domain tool named JACoP (http://rsb.info.nih.gov/ij/plugins/track/jacop.html) that groups the most important ICCB tools and allows the researcher to compare the various methods with one mouse-click. Furthermore, an object-based tool called three-dimensional object counter (http://rsb.info.nih.gov/ij/plugins/track/objects.html) is also available that may be used for object-based colocalization analysis. These tools process image stacks and allow an automated colocalization analysis in the three-dimensional space. To introduce these tools and their utility in colocalization analysis we will give a general overview on the roots of ICCB and object-based methods.

For this purpose, we have compared four different possible subcellular colocalization situations (Fig. 4). A complete

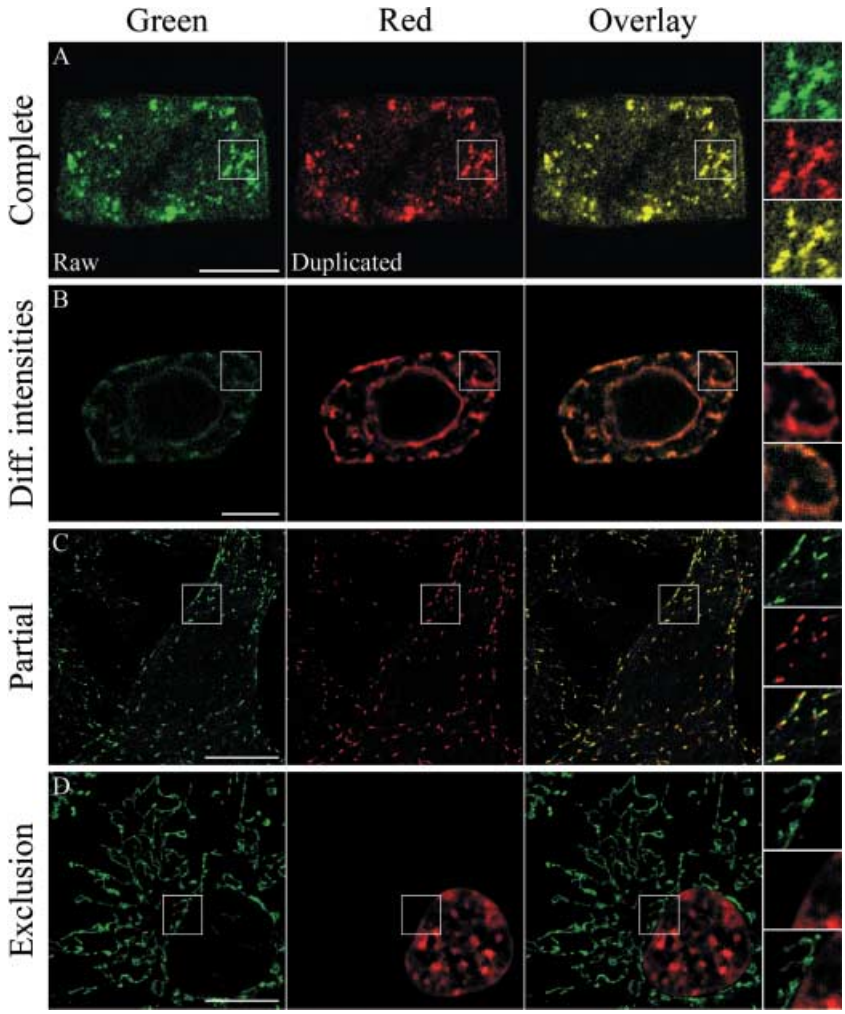

Fig. 4. Reference images for colocalization analysis. Images for colocalization analysis were acquired from fixed maize root cells with Golgi staining (A) (Boutté *et al.*, 2006) or endoplasmic reticulum staining (B) (Kluge *et al.*, 2004) and on fixed mammalian HeLa cells with microtubule plus-end tracking proteins EB1 and CLIP-170 staining (C) (Cordelières, 2003), and nuclear and mitochondrial staining (D). Scale bars, 10 μm. These images illustrate the four commonly encountered situations in colocalization analysis. (A) Complete colocalization. (B) Complete colocalization with different intensities. (C) Partial colocalization. (D) Exclusion. Grey level images of the green and red image pairs (A–D) were used for subsequent treatments with Image J. A zoomed view of the insets is shown on each side of the colour panels.

colocalization situation has been modelled by duplicating a raw image of a Golgi staining in a plant cell (as in Boutté *et al.*, 2006) and assigning it to two different colour channels (Fig. 4A, Raw and Duplicated). Another situation, complete colocalization with different intensities, is given by the colabelling of the endoplasmic reticulum with two endoplasmic reticulum-specific antibodies (as in Kluge *et al.*, 2004; Fig. 4B). A partial colocalization situation is shown by the colabelling of mammalian cells with different microtubule plus-end tracking proteins (Cordelières, 2003; for reviews, see Schuyler & Pellman, 2001; Galjart, 2005) (Fig. 4C). Exclusion of fluorescent signals has been achieved by staining mitochondria and the nucleus in mammalian cells (Fig. 4D). To investigate the influence of fluorescence background or photonic noise on colocalization analysis with JACoP, we added different levels of random noise to the complete colocalization image pair (image data not shown). The signal-to-noise ratios in these images were calculated and varied from 12.03 to 3.52 dB.

Correlation analysis based on Pearson's coefficient

The ICCB tools mainly use statistics to assess the relationship between fluorescence intensities. A wealth of colocalization analysis software now available as part of basic image-analysis tools or more specialized imaging-analysis software is based on ICCB analysis. This is mainly due to the relative ease of implementing the software. In this case, statistical analysis of the correlation of the intensity values of green and red pixels in a dual-channel image is performed. This is mostly done using correlation coefficients that measure the strength of the linear relationship between two variables, i.e. the grey values of fluorescence intensity pixels of green and red image pairs.

Pearson's coefficient. A simple way of measuring the dependency of pixels in dual-channel images is to plot the pixel grey values of two images against each other. Results are then displayed in a pixel distribution diagram called a scatter plot (Fig. 5) or fluorogram. The intensity of a given pixel in the green image is used as the x-coordinate of the scatter plot and the intensity of the corresponding pixel in the red image as the y-coordinate. In some software the intensity of each pixel represents the frequency of pixels that display those particular red and green values in the fluorogram image. Leaving aside noise and low background, we will firstly examine the scatter plot to see if there are numerous pixels with only one significant signal (Fig. 5E). Secondly, where both signals are present, we shall describe their relationship as a strong, lower, weak or non-existent correlation that may be positive or negative. If we consider that the labelling of both fluorochromes is proportional to the other and the detection of both has been carried out in a linear range, the resulting fluorogram pattern should be a line. The slope would reflect the relative stoichiometry of both fluorochromes, modulated by their relative detection efficiencies. In practice in a complete colocalization situation, dots on the diagram appear as a cloud centred on a line (see Fig. 5A). The spread of this distribution with respect to the fitted line may be estimated by calculating the correlation coefficient, also called Pearson's coefficient (PC). As most ICCB tools are based on the PC or its derivatives, we will introduce it here in detail.

The linear equation describing the relationship between the intensities in two images is calculated by linear regression. The slope of this linear approximation provides the rate of association of two fluorochromes. In contrast, the PC provides an estimate of the goodness of this approximation. Its value can range from 1 to −1, with 1 standing for complete positive correlation and −1 for a negative correlation, with zero standing for no correlation. This method has been applied to measure the temporal and spatial behaviour of DNA replication in interphase nuclei (Manders *et al.*, 1992). We used the JACoP tool to analyse the Pearson's correlation coefficients and to visualize the corresponding scatter plots of the four different colocalization situations described in Fig. 4. Figure 5(A) shows the scatter plot with the dots on the diagram appearing as a cloud centred on a line in the case of complete colocalization. The PC approaches 1 in this case. A difference in the intensities of the green image with still completely colocalized structures results in a rotation of the dotted cloud towards the red axis (Fig. 5B). As a consequence, the fitted line changes its slope and comes closer to the axis of the most intense channel. We can state that colocalization is observed whenever both signals are significant but that a subpopulation of purely red pixels has appeared because of poor sensitivity in the green channel. In the partial colocalization situation the dots of the scatter plot form a rather uniform cloud with a PC of 0.69 (Fig. 5C). Mutual exclusion of the fluorescent signals shows scattered distributions of the pixels close to both axes (Fig. 5D) and a negative PC.

Scatter plots and PCs point to colocalization especially where it is complete (Fig. 5A and B); however, they rarely discriminate differences between partial colocalization or exclusion, especially if images contain noise. The influence of noise and bleed-through on the scatter plots and PCs is shown in Fig. 5(A*) and (F) (black bars). Random noise has been added to the image pairs of Fig. 4(A) and is recognizable by the shapeless cloud of dots near the origin (Fig. 5A*). As a consequence, the PC will decrease and finally tend to zero as more noise is added (Fig. 5F, black bars). This demonstrates the sensitivity of PC to background noise and hence to thresholding. These results show that an evaluation of colocalization events using PCs alone may be ambiguous, as values are highly dependent on noise, variations in fluorescence intensities or heterogeneous colocalization relationships throughout the sample (Fig. 5A–C). Noise and background must be removed. Moreover, the coefficient will soon be dominated, not by the central phenomenon, but by the perimeter given to the analysis (the near-threshold events). Values other than those close to 1 and especially mid-range coefficients (–0.5 to 0.5) do not allow conclusions to be drawn.

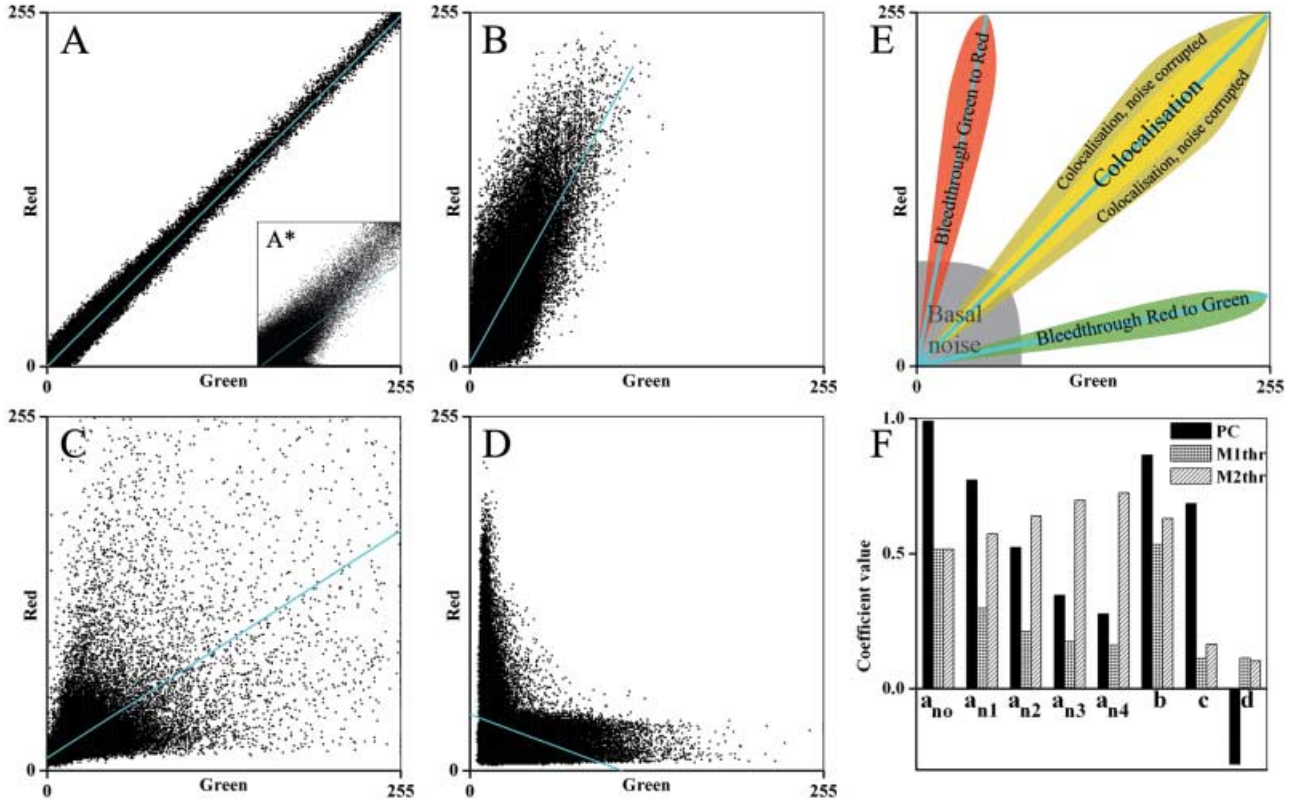

Fig. 5. Colocalization analysis with JACoP; Pearson and Manders, scatter plots and correlation coefficients. Scatter plots (A–D) correspond to the colocalization events as shown in Fig. 4. (E) Model scatter plot explaining the effects of noise and bleed-through. (F) Pearson's and Manders' coefficients in the different colocalization situations. A complete colocalization results in a pixel distribution along a straight line whose slope will depend on the fluorescence ratio between the two channels and whose spread is quantified by the Pearson's coefficient (PC), which is close to 1 as red and green channel intensity distributions are linked (F, a_{n0}, black bar). (B) A difference in fluorescence intensities leads to the deflection of the pixel distribution towards the red axis. Note that the PC diminishes even if complete colocalization of subcellular structures is still given (F, b, black bar). (C) In a partial colocalization event the pixel distribution is off the axes and the PC is less than 1 (F, c, black bar). (D) In exclusive staining, the pixel intensities are distributed along the axes of the scatter plot and the PC becomes negative (F, d, black bar). This is a good indicator for a real exclusion of the signals. (E) The effect of noise and bleed-through on the scatter plot is shown in the general scheme. (F) The influence of noise on the PC was studied by adding different levels of random noise (n1–n4)* to the complete colocalization event (A = n0, no noise). (F) Note that the PC (black bar) tends to 0 when random noise is added to complete colocalizing structures. The inset (A*) in (A) shows the scatter plot for the n2 noise level. Note that all of the mentioned colocalization events (A–D) may only be detected faithfully once images are devoid of noise. (F) Manders' coefficients were calculated for (A–D). The thresholded Mander's tM_1 (cross-hatched bars) and tM_2 (diagonal hatched bars) are shown. Compare complete colocalization (a_{n0}), complete colocalization with random noise added (a_{n1}–a_{n4}), and complete colocalization with different intensities (b), partial colocalization (c) and exclusion (d). Note that the original Manders' coefficients are not adapted to distinguish between these events, as they stay close to 1 for all situations (not shown). *Signal-to-noise ratios are: n1 = 12.03 dB, n2 = 6.26 dB, n3 = 4.15 dB and n4 = 3.52 dB.

This also applies when looking at images corrupted by bleed-through. A thin cloud of correlated pixels will appear on the scatter plot, close to one or both axes (data not shown). As a consequence, PC will tend to −1 or 1 although not representing a biological correlation.

Although provided in most standard image-analysis software packages, scatter plots in combination with the PC only give a first estimate of colocalization. They are especially useful for initial identification of diverse relationships (correlations, bleed-through, exceptional coexpression of signals) and for examination of complex overlays through the windows (regions of interest) so defined. However, they are not sufficient to evaluate colocalization events rigorously. The PC defines the quality of the linear relationship between two signals but what if the sample contains two or more different stoichiometries of association? The linear regression will try to fit the segregated dot clouds as one, resulting in a dramatic decrease of the PC. The best alternative would be to fit dot clouds by intervals, resulting in several PCs for a single pair of images.

Manders' coefficient. Manders' overlap coefficient is based on the Pearson's correlation coefficient with average intensity values being taken out of the mathematical expression (Manders *et al.*, 1992). This new coefficient will vary from 0 to 1, the former corresponding to non-overlapping images and the latter reflecting 100% colocalization between both

images. M_1 is defined as the ratio of the 'summed intensities of pixels from the green image for which the intensity in the red channel is above zero' to the 'total intensity in the green channel' and M_2 is defined conversely for red. Therefore, M_1 (or M_2) is a good indicator of the proportion of the green signal coincident with a signal in the red channel over its total intensity, which may even apply if the intensities in both channels are really different from one another. This definition could reveal both coefficients to be perfect for colocalization studies. Unfortunately, this is only true if the background is set to zero. Furthermore, it is not possible to distinguish between complete and partial colocalization situations with the M_1 and M_2 coefficient. The Manders' coefficient is very sensitive to noise. To circumvent this limit, M_1 and M_2 may be calculated setting the threshold to the estimated value of background instead of zero (Fig. 5F, cross-hatched and diagonal hatched bars). When noise or cross-talk are present, the automatically retrieved threshold may be too high, leading to the loss of valuable information. In this case, noise and cross-talk must be corrected before calculating the coefficients.

Costes' approach. Recently, a statistical significance algorithm based on the PC has been introduced (Costes *et al.*, 2004). The Costes' approach is performed in two subsequent steps. Firstly, the correlation in different regions of the two-dimensional histogram is taken into account to estimate an automatic threshold and the PC of this thresholded image pair is calculated. To calculate this automatic threshold, limit values for each channel are initialized to the maximum intensity of each channel and progressively decremented. The PC is concomitantly calculated for each increment. The final thresholds are then set to values that minimize the contribution of noise (i.e. PC under the threshold being null or negative). As a second step, Costes *et al.* (2004) introduced a new statistical analysis based on image randomization and evaluation of PC. The authors pointed out that a single image reflects a particle distribution with sizes above optical resolution. These particles appear as a collection of adjacent pixels with intensities correlated to their neighbours. The intensity distribution depends on the PSF of the acquisition system and the approximate particle size may be calculated using the full width at half maximum of the fluorescence intensity curve. The full width at half maximum defines the area over which a signal belonging to a single particle is spread out, given the fact that the particle size is convolved by the PSF of the optical system. The authors created a randomized image by shuffling pixel blocks with the dimensions defined by the full width at half maximum for the image of the green channel. This process is done 200 times for a single image and the PC is calculated each time between the random images of the green channel and the original image of the red channel. The PC for the original non-randomized images is then compared with the PCs of the randomized images and the significance (*p*-value) is calculated. The *p*-value, expressed as a percentage, is inversely correlated to the probability of obtaining the specified PC by chance (i.e. on randomized image pairs). This value is calculated as the integrated area under the PC distribution curve, from the minimum PC value obtained from randomization to the PC obtained from original images (see Fig. 6). This method introduces for the first time a statistical comparison that may exclude colocalization of pixels due to chance.

We performed this two-step analysis with JACoP for the four colocalization events mentioned earlier. However, for clarity we only show the scatter plot and image pairs analysed for the partial colocalization event (Fig. 6). We obtained a scatter plot that is divided into four differentially coloured zones by horizontal and vertical lines that represent the borders of the automatic thresholds for the red and green channel, respectively (Fig. 6A). The PC is 0.69. Subsequently, we created a set of 200 randomized images (see Fig. 6B, randomized green image) from the green image and calculated the colocalization map and the *p*-value (Fig. 6B). An overlay of green and red channels with the mask of the colocalizing pixels in white (Fig. 6B, colocalization map) gives a topological map of co-localization distribution. The PC calculated earlier has a *p*-value of 100%, suggesting that colocalization in the regions masked in white is highly probable.

Figure 6(C) and (D) show the confidence interval, i.e. the range of PC variation obtained from randomized images (C, curve; D, grey bars), in comparison to the PCs obtained for the initial set of images (red lines and bars). Surprisingly, the original PC is above the upper boundary of the confidence interval in the complete colocalization situation, in complete colocalization with different intensities and in partial colocalization (Fig. 6D, a_{n0} to c). This means that all of those situations may be considered as true colocalization cases. As expected in the case of exclusion, the PC is below the lower boundary of the interval and the *p*-value is equal to 0% (Fig. 6D, d). It seems that this method points out true colocalization even when images are corrupted by high levels of noise (Fig. 6D, a_{n1}–a_{n4}). However, the Costes' approach may reach its limits when increasing the statistical parameters of noise and especially the SD of noise. The confidence interval may encompass the original PC, which may impair a prognostic of a true colocalization, as the *p*-value is dependent on the distance between the lower boundary of the interval and the original PC value. In that particular situation, the colocalization diagnostic may not give rise to a valid conclusion.

Although providing a first statistical estimate of colocalization, Costes' approach is also highly dependent on the way in which the test is set up. The authors initially proposed 200 randomization rounds to obtain a significant statistical distribution with more randomization leading to more reliable elimination of false positives.

Van Steensel's approach. Another development based on PC has been proposed for colocalization analysis using, as an example, glucocorticoid and mineralocorticoid receptors in

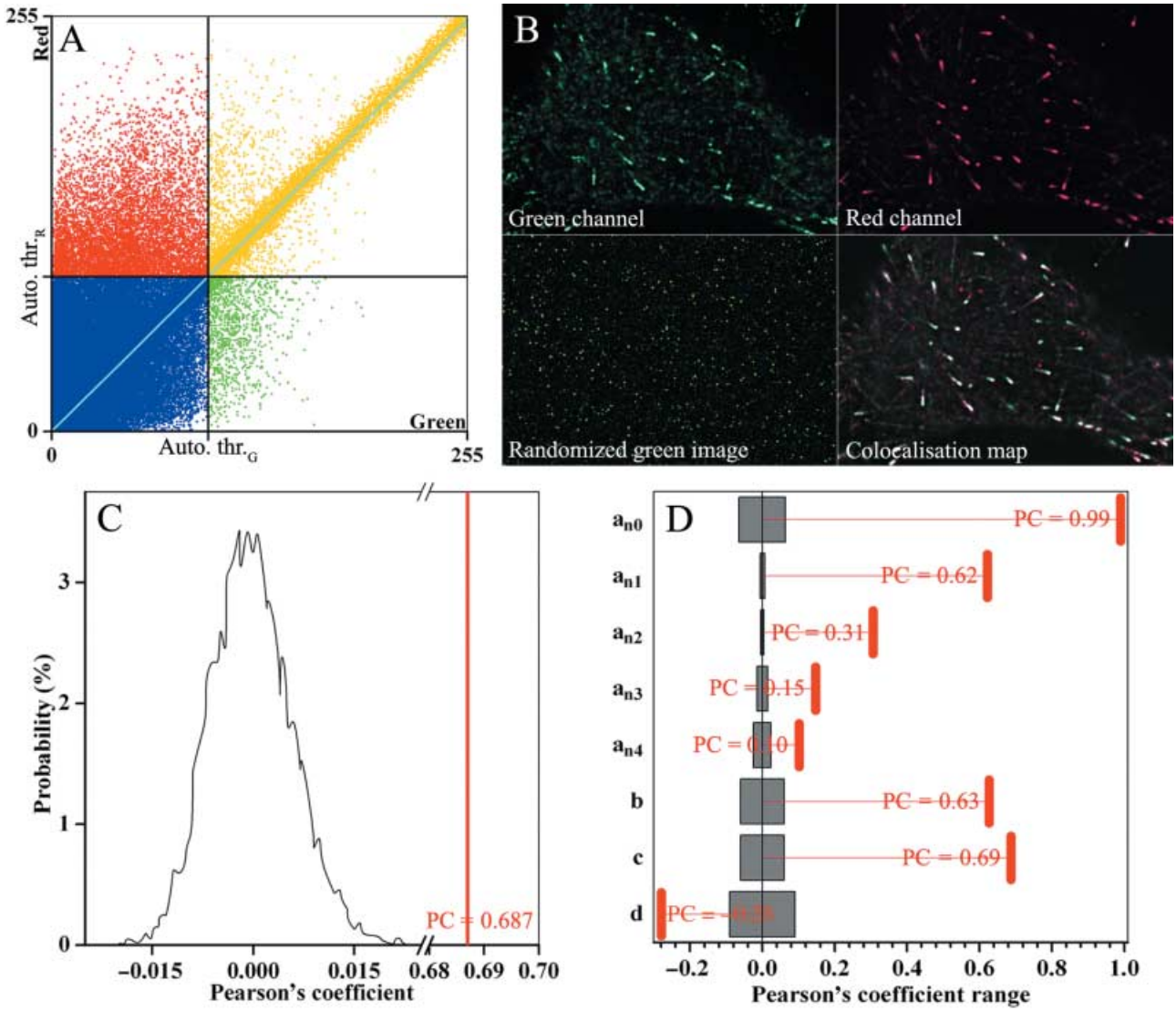

Fig. 6. Colocalization analysis with JACoP; Costes. (A) Scatter plot of a partial colocalization situation (such as Figs 4C and 5C). We distinguish four regions of interest (red, yellow, green and blue overlay); the yellow region represents all pixels above the dual automatic thresholds; the red region represents all pixels with red channel intensities over the automatic threshold and the green channel represents intensities below the automatic threshold. The green region represents pixels with green pixels over and red pixels below threshold and the blue region designates pixels under the threshold in both channels. (B) A green and red image pair (Green and Red channel) was used for image randomization, creation of a colocalization map and subsequent *p*-value calculation. A set of 200 randomized images was created from the green channel image (randomized green image is one example out of 200). Co-localizing pixels are shown as a white overlay on the green and red channel merge (Colocalization map). (C) Plot of the distribution of the Pearson's coefficients (PCs) of randomized images (curve) and of the green channel image (red line). The red line indicates the PC and the curve shows the probability distribution of the PCs of the randomized images. Note that the *p*-value for this analysis was 100% indicating a high probability of colocalization. (D) Range of PCs obtained from randomized images (grey bars, mean value ± SD) compared with the PC obtained for the initial set of images (red lines) in cases of complete colocalization events (a) with different levels of noise added (a_{n0}–a_{n4}), different intensities (b), partial colocalization (c) and exclusion (d). The *P*-values were 100% for (a–c) and 0% for (d).

the nuclei of rat hippocampus neurones (Van Steensel *et al.*, 1996). These receptors are concentrated in punctate clusters within the nucleus that partially colocalize. The authors applied a cross-correlation analysis by shifting the green image in the x-direction pixel per pixel relative to the red image and calculating the respective PC. The PC is then plotted as the function of δx (pixel shift) and the authors thus obtained a cross-correlation function. We performed the analysis on the four different colocalization situations with the following results. Completely colocalizing structures peak at $\delta x = 0$ and show a bell-shaped curve (Fig. 7A). A difference in fluorescence intensity leads to a reduction of the height of the bell-shaped curve,

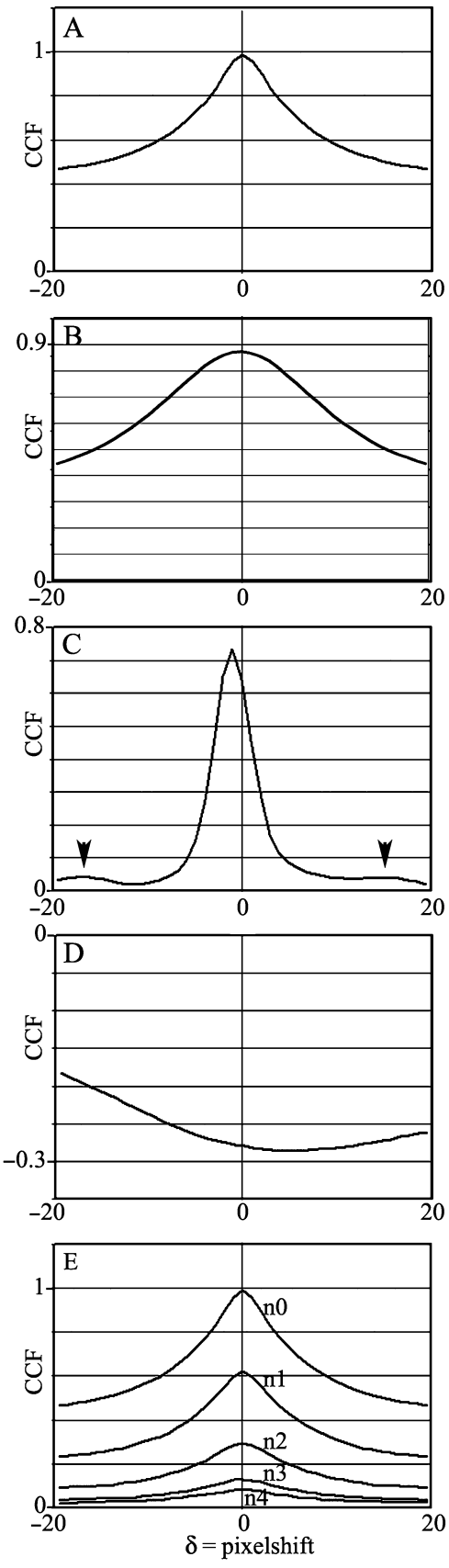

whereas the peak is still at $\delta x = 0$ (Fig. 7B). Partially overlapping structures show a peak aside of $\delta x = 0$ (Fig. 7C). Structures that are mutually excluded from each other show a dip at $\delta x = 0$ (Fig. 7D).

The cross-correlation function allows ready discrimination between the different colocalization events. However, it has the major drawback that it is only valuable for small and isotropic particles, as it may vary depending on their orientation relative to the selected shift axis. The cross-correlation function calculation allows an estimation of the dimensions of the particles, as the width of the bell-shaped curve at half maximum reflects the approximate particle size convolved by the PSF of the optical system.

Li's approach. The work of Li *et al.* (2004) is of particular interest in the search for an interpretable representation of colocalization to discriminate coincidental events in a heterogeneous situation. They first assumed that the overall difference of pixel intensities from the mean intensity of a single channel is equal to zero, $\sum_{n\ pixels}(A_i - a) = 0$ and $\sum_{n\ pixels}(B_i - b) = 0$ with the upper-case character being the current pixel's intensity and the lower-case character being the current channel's mean intensity. As a consequence, the product of the two equalities should tend to zero. Now if we consider colocalizing pixels this product should be positive as each difference from the mean is of the same sign. The differences of intensities between both channels are scaled down by fitting the histogram of both images to a 0–1 scale. The intensity correlation analysis results are then presented as a set of two graphs, each showing the normalized intensities (from 0 to 1) as a function of the product $(A_i - a)(B_i - b)$ for each channel (Fig. 8). In this representation the x-axis reflects the covariance of the current channel and the y-axis reflects the intensity distribution of the current channel. As previously stated, in the case of colocalization the product $(A_i - a)(B_i - b)$ is positive and therefore the dot cloud is mostly concentrated on the right side of the $x = 0$ line, although adopting a C shape (Fig. 8A, A* and E). Its spread is dependent on the intensity distribution of the current channel as a function of

Fig. 7. Colocalization analysis with JACoP; Van Steensel. (A–D) Cross-correlation functions (CCFs) were calculated (with a pixel shift of $\delta = \pm 20$) for complete colocalization (A), complete colocalization with different intensities (B), partial colocalization (C) and exclusion (D). Completely colocalizing structures peak at $\delta = 0$ (A), even if different intensities of the two fluorescent channels are present (B). Partially colocalizing structures show a shift away from 0 in the maximum of the CCF (C). When the region of interest is quite crowded, shifting one image with respect to another may enhance the probability of obtaining colocalization, therefore slightly increasing the Pearson's coefficient (arrowheads). Exclusion of structures leads to an inversion of the CCF, which shows a dip around $\delta = 0$ (D). (E) Effect of random noise (n1–n4) on the CCF in comparison to A = n0. Random noise results in a decrease of the maximum while full width at half maximum increases; it is still possible to identify the colocalization event.

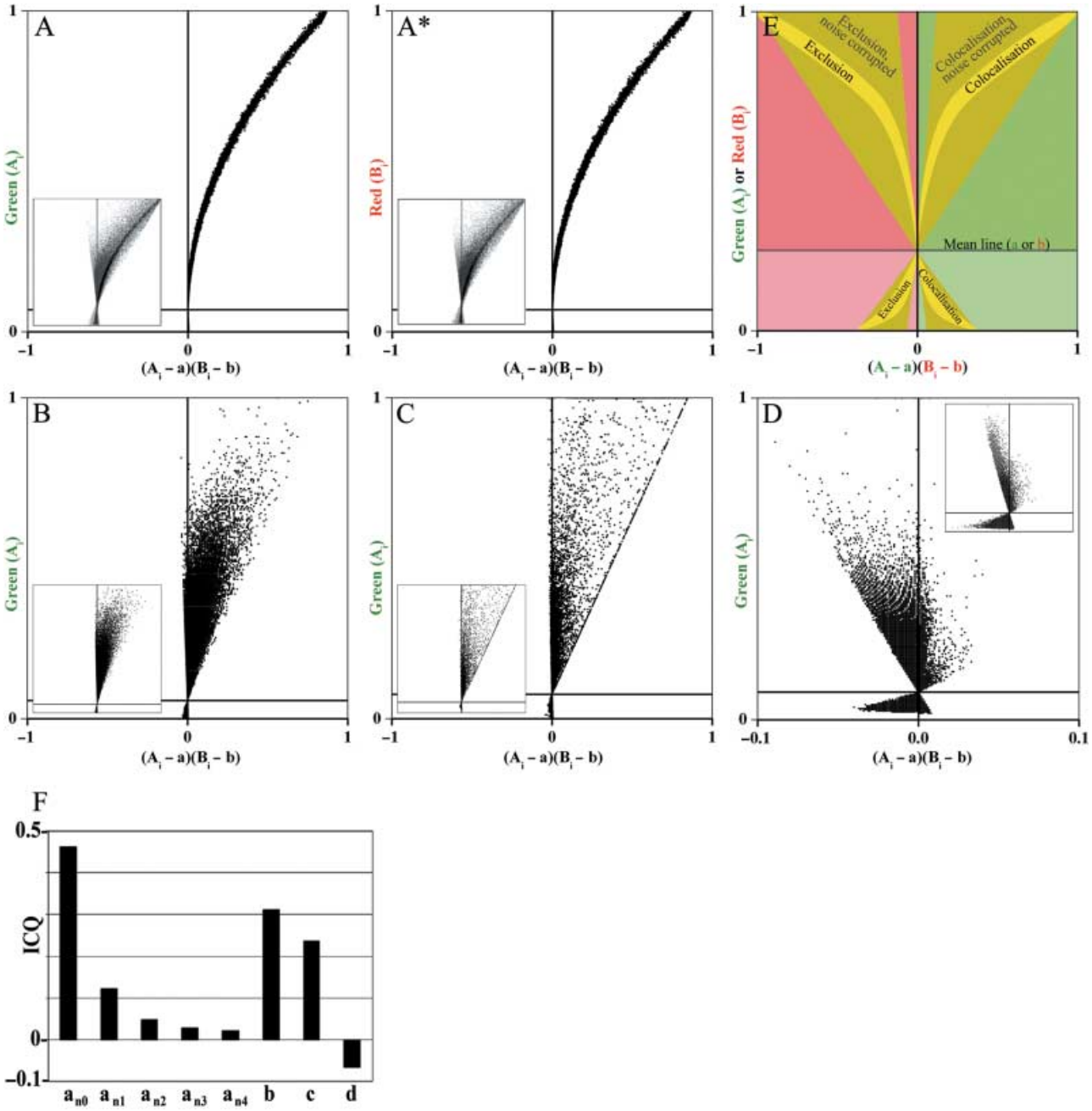

Fig. 8. Colocalization analysis with JACoP; Li. (A–D) Intensity correlation analysis (ICA) was performed for complete colocalization (A and A*), complete colocalization with different intensities (B), partial colocalization (C) and exclusion (D). (A–D) ICA of the green channel; (A*) and insets of (B–D) ICA of the red channel. The x-value is dependent on covariance of both channels and the y-value reflects the intensity distribution of the current channel. Pixels with values situated left of the x = 0 line do not colocalize or have inversely correlated intensities, whereas pixels situated on the right side colocalize (see E for details). The horizontal line indicates the position of the mean intensity of the current channel allowing the visual estimate of the spread of intensity distribution with respect to the mean value. (A and A*) Complete colocalization results in a C-shaped curve on the right side of both graphs. The addition of random noise leads to the expansion of the C-shaped curve (A and A*, insets, grey dots). (B) In the case of complete colocalization with different intensities the pixel cloud is shifted up or down the ordinate axis, with most pixels situated on the positive side of the graph. (C) Partial colocalization results in a loss of valuable information as the minority of colocalized pixels fail to form a strong identifiable dense cloud. (D) Exclusion of the fluorescent signals results in a pixel distribution with most of the pixels found on the left side of the plot. Pixels with low intensities that are found on the right side are due to noise. (E and F) Intensity correlation quotient (ICQ) values, which are dependent on the proportion of pixels on the left side of the x = 0 line to the total number of pixels, are plotted for compete colocalization events (a) with different levels of noise added (a_{n0}–a_{n4}), different intensities (b), partial colocalization (c) and exclusion (d).

the covariance of both channels' intensities. This becomes clearer when adding random noise to the completely colocalizing images. Compare the C-shaped curve of complete colocalization (Fig. 8A and A*) with the expanded curve when noise is added (Fig. 8A and A*, insets). Note that the addition of noise may also result in the spread of dots to the left side of the graph. In the case of complete colocalization with different intensities, the pixel cloud in the red channel is shifted up the ordinate axis (Fig. 8B). Non-colocalizing pixels are found on the left side of the plot. Partial colocalization spreads the pixel cloud within the right side of the plot (Fig. 8C). Mutual exclusion of the fluorescent signals results in a pixel distribution with most of the pixels found on the left side of the plot (Fig. 8D). Pixels with low intensities that are found on the right side are due to noise randomly coincident between the two channels.

For random distribution of fluorescent signals, badly deconvolved images or, in the case of high contamination by noise, a rather symmetrical hourglass-shaped distribution of dots is observed (Fig. 8E). In these cases, the result is quite difficult to interpret and therefore the intensity correlation quotient might be calculated. This is defined as the ratio of positive $(A_i - a)(B_i - b)$ products divided by the overall products subtracted by 0.5. As a consequence, the intensity correlation quotient varies from 0.5 (colocalization) to −0.5 (exclusion), whereas random staining and images impeded by noise will give a value close to zero (Fig. 8E and F). The development of this graphical method interpreting image sets based on their respective intensities is a step forward compared with the previously described scatter plots as it allows a direct identification of colocalization and exclusion. However, it is still a global method that does not allow conclusions in intermediate cases.

Object-based analysis

The main disadvantage of the ICCB tools introduced so far is that no spatial exploration of the colocalized signal is possible. All methods previously described rely on individual pixel coincidence analysis, considering that each pixel is part of the image and not part of a unique structure. Although giving a global estimation of colocalization, their numerical indicators suffer from the composite nature of the images, which is a patchwork of both structures and, even though minimized, background.

There are several possibilities for measuring and evaluating subcellular structures by object-based approaches. The methods depend on the nature of the colocalization event but also on the size, form and intensity distribution of the fluorescent signal. Concerning the nature of colocalization situations, we have to distinguish between those with two markers occupying the same space on all subcellular structures (complete colocalization, such as Fig. 4A) or on some subcellular structures (partial volumetric colocalization, such as Fig. 4C) and between incomplete colocalization situations with two markers overlapping partially on all or some subcellular structures (partial topological colocalization, such as in Bolte *et al.*, 2004b). It is recalled that any entity below optical resolution will occupy at least $2 \times 2 = 4$ pixels (or even $3 \times 3 = 9$ pixels in the case of sampling at 2.3 pixels per resolution unit) in the two-dimensional space so no discrimination can be expected between subresolution objects. However, respecting the Nyquist sampling criterion, an object may be positioned with an error of ~70 nm (Webb & Dorey, 1995). Biological structures are three-dimensional and it has already been mentioned that the discrepancy between lateral and axial resolution of optical microscopes leads to a distortion of the object along the z-axis. Therefore, object-based analysis needs to be carried out in the three-dimensional space by taking account of the degree of distortion by the optical device.

A method of choice to measure colocalization on structures with a size close to or larger than the resolution limit and especially in the case of partial volumetric colocalization relies on a manual identification of structures and a subsequent measurement of their fluorescence intensity curves. This is done by drawing a vector through these structures and plotting the fluorescence intensities for the green and red channel against the length of the vector. This can be done in any image software and is basically a line scan through a two-dimensional image of a fluorescent object, representing the fluorescence intensities along a vector traced across the object. Colocalization is present when the true overlap distance of the fluorescence intensity curves at mid-height is larger than the resolution of the objective used for image acquisition (Fig. 9B). Fluorescence intensity profiles of overlapping subcellular structures should give similar overlap results in those successive single sections from an image stack representing the two structures and matching the z-resolution of the optical system used. This method has been applied to show the partial colocalization of plant Golgi stacks and prevacuolar compartments (Bolte *et al.*, 2004b). Although powerful on colocalization estimation, this method is time consuming and will only be applicable to a limited number of structures as positioning of the vector is interactive. Furthermore, mispositioning of the vector may lead to underestimation of colocalization events. Moreover, this method is likely to work only on isotropic, solid structures such as doughnut-shaped or elongated structures.

One step forward in colocalization quantification relies therefore on its local estimation based on object identification and delineation. This challenging area of image processing is known as image segmentation. Although many techniques exist, we will only describe segmentation procedures that have already been used for colocalization analysis.

Looking for objects: basic image segmentation. In an optimal situation, pixels deriving from noise should have lower intensities than pixels deriving from structures. A first step to identifying these structural pixels as objects may be achieved by applying a

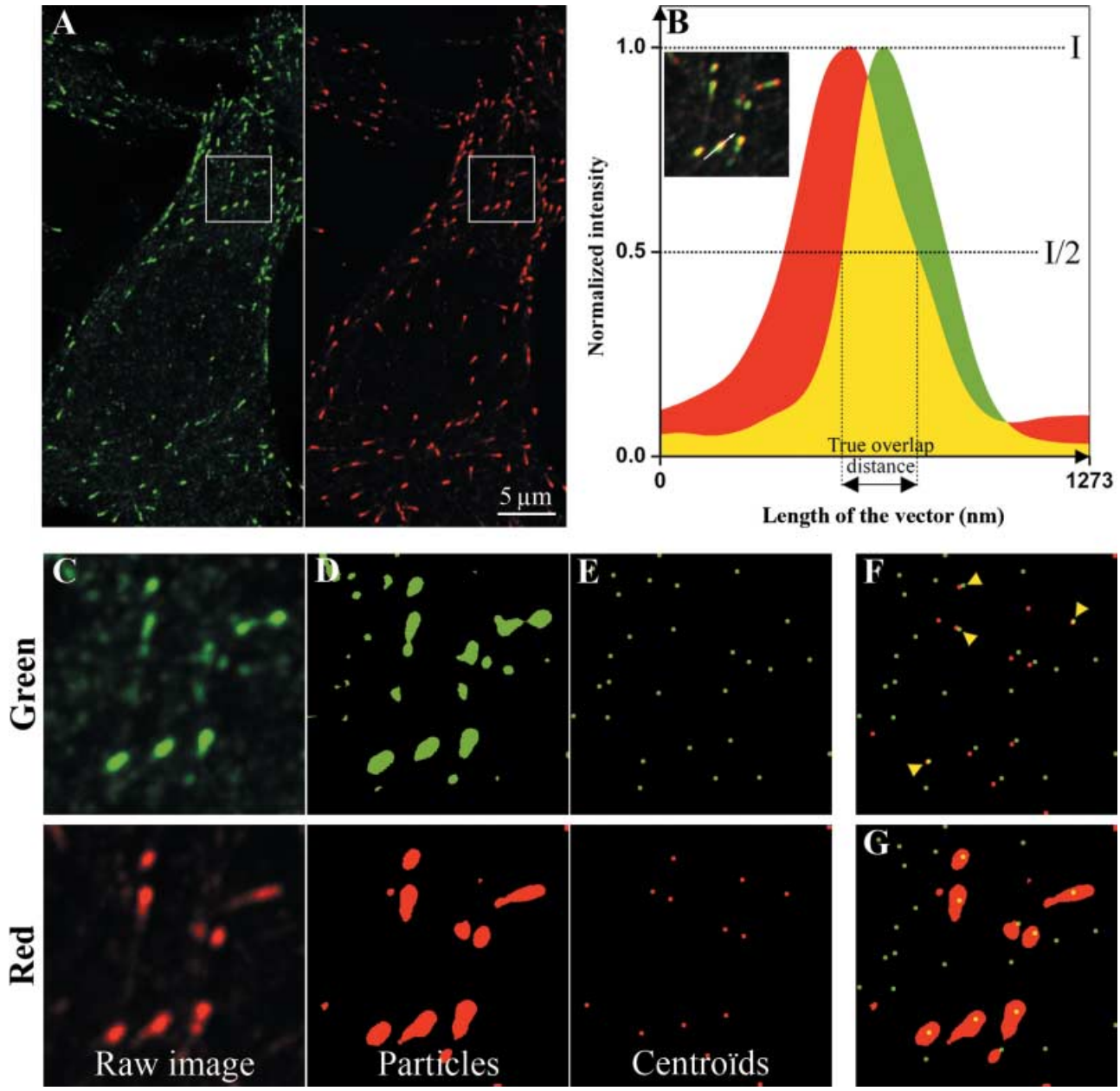

Fig. 9. Object-based colocalization analysis by fluorescence intensity profiles and connexity analysis. The analysis was performed on grey level images of partially colocalizing fluorescent structures (as shown in Fig. 4C). (A) Raw images showing partial colocalization of fluorescent subcellular structures with green (left panel) and red (right panel) channels. (B) Inset of overlay of raw images as shown in (A) and intensity curves measured along a vector across two fluorescent structures (white arrow). (C) Magnified view of the inset shown in (B). The segmentation process by connexity analysis results in particle (D) and centroid (E) detection. (F) Nearest-neighbour distance approach by merging green and red channel centroids. Colocalization is present when centroids have distances below optical resolution (yellow arrowheads). (G) Merged view of centroids of the green image (E) and particles of the red image (D) illustrates the overlap. Note that the overlap method doubles apparent colocalization events.

threshold to the image; all pixels with intensities above a limit value (threshold) will be considered to be part of an object. In most cases, this threshold value may be defined manually following visual inspection (Fig. 9C and D). It is also possible to apply an automatic threshold as we have already seen (Costes *et al.*, 2004). Noise is not fully eliminated as it remains within structures but at least two main areas are now defined on the image, regions where structures (and noise) are present and regions where only noise is present.

Although thresholding enables one to distinguish between background and objects, one more step is required to delineate each structure. As a first approximation, the limit of an object

may be seen as a sudden variation of the pixel intensities when performing a line scan. The first derivative of this line scan will be zero as long as the intensities in the background area, or inside a uniformly labelled structure, are almost constant and different from zero when passing from background to object (or from object to background). A new image may be created using these values to show enhanced edges. This so-called edge detection may be achieved by the use of filters that are available in most common imaging software, namely Sobel and Laplacian filters (Sobel, 1970; Ronot & Usson, 2001). It is, however, important to note that these filters have their limits. Structures with non-uniform fluorescence intensity distribution may lead to an artefactual detection of concentric edges. Moreover, such filters will highlight the outline of the structure but give no information on the structural content.

Other methods may be used to separate structures from background while keeping information on their fluorescence intensities as intact as possible. The first approach is based on the topological relationship of adjacent pixels, a step named connexity analysis (implied in the three-dimensional object counter). Briefly, this process consists of systematic inspection of the neighbourhood (8 pixels in two-dimensions and 26 voxels in three-dimensions) of the current pixel (reference pixel); all adjacent pixels with intensities above the threshold limit are considered to be part of the same structure as the reference pixel. Each pixel is then tagged with a number, with all pixels of the same structure carrying the same tag. A pixel lacking at least one of its neighbours is considered to be at the edge of the structure. This procedure results in two images, one carrying the intensity information (Fig. 9C, raw image) and the other representing individualized structures (Fig. 9D, particles). This method applies whatever the size and shape of the target structures are and requires no *a-priori* knowledge of those parameters. In the case where all structures have the same shape and size, another approach may be used. The top-hat filter (Meyer & Beucher, 1990) is a morphological filter that may be utilized to look for structures matching a precise shape called the structuring element. The top-hat filter slightly affects the pixel intensities but has the advantage of correcting uneven illumination by bringing the foreground intensity inside the structuring element back to the minimum value. Its selectivity on the structural features implies that part of the information may be left aside in the subsequent analysis. By performing connexity analysis or top-hat filtering, the segmentation of structures may not be perfect. Structures may still stick together and may be individualized by a further step called watershed filtering that will split apart the joint structures by highlighting their common boundaries (for review, see Roerdink & Meijster, 2000).

After segmentation it is possible to determine centroids and intensity centres from the structures. This process may be carried out automatically in the three-dimensional space (Fig. 9E). Centroids are the geometrical centres of objects including the global shape of the structures. Intensity centres take into account the distribution of fluorescence intensity of the object. In the case of geometrically isotropic structures, both centroids and intensity centres may be coincident but this is not obligatory, as fluorescence distribution might be anisotropic. The above-mentioned segmentation procedures and the parameters retrieved may be used differentially to estimate the degree of object-based colocalization of two markers as will be described in the following.

Looking for coincidence of discrete structures: object-based colocalization. One way to measure colocalization is to compare the position of the three-dimensional centroids or intensity centres of the respective subcellular structures of the two colour channels. Those positions may be displayed in an overlay window (Fig. 9F) and their respective x, y, z coordinates will then be used to define structures separated by distances equal to or below the optical resolution. As a consequence, we will conclude that both structures colocalize if their distance is below optical resolution. This method has been applied to prove the Golgi association of AtPIN1, the plant auxin efflux carrier. Two objects were considered to colocalize if the distance between their centres was less than the resolution of the microscope used (Boutté *et al.*, 2006). A similar approach has been used to study the complex formation among membrane proteins underlying the plasma membrane of mammalian cells (Lachmanovich *et al.*, 2003). The authors included top-hat filtering and watershed processing to separate small round-shaped vesicles. After segmentation, centroids were calculated and the distances between objects from the green and red channel images were measured. This process was called 'nearest-neighbour distance approach'. As the number of objects may differ between two channels, the measurement has to be set to select objects from the channel with fewer objects and to search for the nearest neighbour from the channel with more objects. The degree of colocalization is then calculated from the percentage of objects in the first channel colocalizing with objects from the second channel, divided by the total number of all objects from the first channel.

Lachmanovich *et al.* (2003) tested the significance of the colocalization results against the degree of colocalization in randomized images, produced as already described (Costes *et al.*, 2004). The use of randomized images as reference allowing statistical evaluation of the object-based approach is indeed a step forward and adds to the validity of the result. However, the measurement of centroid distances by the nearest-neighbour distance has two main limits. Firstly, the segmentation procedures select elements that meet pre-defined criteria. The method is thus restricted to rather isotropic structures and may lead to under-estimation of colocalization. Structures with shapes deviating from the pre-fixed criterion may be incorrectly discarded. Secondly, the use of centroids to define objects may result in under-estimation of colocalization due to anisotropic intensity distributions within the structures if the

objects are larger than the optical resolution or if they differ in size between the two colour channels. The first case can be ruled out by calculating intensity centres rather than centroids. For the second case, Lachmanovich *et al*. (2003) developed another approach called the overlap approach; objects in the green and red channels colocalize if the centroid of an object of the green channel falls into the area covered by an object of the red channel (Fig. 9G). The degree of colocalization is then given by the percentage of green objects colocalizing with red objects in the area of interest. Counting the number of green centroids matching red object areas and red centroids matching green object areas resulted in two percentages of overlap. These percentages were compared with a random distribution obtained as described before and thereby allowed a statistical evaluation of colocalization. The overlap method enhances the probability of matching structures, as matching a centroid to an object area is more probable than matching two centroids. This method may work on categories of objects and therefore gives information on a single class of structures rather than giving an overall estimate of colocalization. By reiterating the analysis on the same images with differential settings of top-hat filtering or other means of segmentation, one may obtain information on different classes of objects. We have automated the analysis of centroids and intensity centres with the three-dimensional object counter plugin that may be combined with several image-segmentation and randomization procedures to provide a first step towards multilevel analysis.

Object-based colocalization implying intensity correlation coefficient-based analysis. Jaskolski *et al*. (2005) proposed a new representation of coincident pixels that has been elaborated after image segmentation based on Sobel filtering. As previously described, a Sobel filter will only highlight the edges of structures, based on detection of rapid intensity variations. The result of this process is a map of edges that will be translated to a binary image by filling the area outside the edges with black pixels (intensity = 0) and the area inside the edges with white pixels (intensity = 1). However, the position of fluorescent structures may differ from one colour channel to the other. As a consequence, to keep track of both sets of structures, the binary images obtained from the green and red channels were combined using the Boolean operation 'OR'. This creates a mask encompassing the relevant structures of both images. By multiplying the original green and red image to the mask, the structures from each colour channel were isolated. This step represents a view of the original image through the filled edge map. As a result, a region of interest only composed of structural pixels present in both channels is obtained, which allows exploration of the correlation of both signals within this region of interest.

The correlation image is then calculated using the normalized mean deviation product (nMDP). In principle this is done using a modification of the intensity correlation analysis method (Li *et al.*, 2004). The numerator is analogous to the abscissa value $(A_i - a)(B_i - b)$ (see 'Correlation analysis based on PC' above), whereas the denominator is used to normalize the nMDP to the product of differences between maximum (A_{max}, B_{max}) to mean intensity (a, b) of both channels $[(A_{max} - a)(B_{max} - b)]$. This allows comparison of the values from one set of images to another.

The numerator of the nMDP is positive for colocalizing pixels as we have previously seen (Li *et al.*, 2004). Jaskolski *et al*. (2005) provide a correlation image (nMDP image) designing non-correlated pixels with values between −1 and 0 with cold colours and correlated pixels with values between 0 and 1 with hot colours. A new numerical indicator (I_{corr}) gives the fraction of pixels with positive nMDPs.

This method of Jaskolski is of particular interest as it combines a direct visualization of colocalization with correlation data. It provides an overall statement based on the global analysis of a region of interest of the image containing the structure. The recapitulative correlation image may help to draw conclusions on structures in a particular region of interest. However, the method is highly dependent on the applicability of the algorithm and the Sobel filtering. The reliability of the segmentation step is crucial and has to be faithfully adapted to the structures investigated. Finally, although this method does not offer any direct statistical validation of the results, as do Costes and Lachmanovich, it proposes a differential diagnostic thanks to the normalization parameter included in nMDP.

Guidelines

We have provided an overview of the most currently used colocalization analysis methods. Although not exhaustive, it points out the advantages and pitfalls of each approach that the cell biologist may use. To help in choosing a method, we will now propose several guidelines for the reader to undertake colocalization analysis.

To get started, colocalization of rather isotropic structures can generally be analysed with the method of Van Steensel *et al*. (1996) thanks to its ability to distinguish between colocalization, exclusion and unrelated signals.

In the event of an evident complete colocalization devoid of noise, simple ICCB methods such as Pearson's approach are efficient at obtaining a numerical estimator from the image. Manders' coefficients may be calculated simultaneously, keeping in mind that comparison of results between datasets may only be applicable if similar acquisition and thresholding conditions are applied. Pearson's and Manders' coefficients are reliable as long as several sets of images have to be compared; however, it is difficult to draw a conclusion from a single dataset. Here, Costes' approach using the creation of a randomized image is useful to evaluate the correlation coefficients obtained in comparison to events occurring due to chance, although it may need more computing time. Subsequent object-based analysis with centroids or intensity centres will tend to amplify the conclusion because they only take into account that fraction of the image occupied by structures.

The absence of colocalization is readily identifiable on Li's intensity correlation analysis scatter plot as a butterfly shape of the dot clouds. As ICCB numerical estimators equal or close to zero do not allow a precise conclusion to be drawn, Li's approach seems to be the only stable method in this situation.

Apart from these extreme colocalization situations, the cell biologist is often confronted with images that are impaired by noise, mixed or partial colocalization. In these cases, a particle-by-particle approach, such as the vector method, will help to obtain a first estimation and the use of other object-based techniques, such as the centroid or intensity centre calculation, may help to identify objects in an automated way. It is also possible to apply differential thresholds that fit different sizes of objects and to subtract particles already analysed from the original to examine various classes of objects.

Conclusions

As biological processes imply the dynamic relocation of proteins between subcellular compartments, it is crucial to perform qualitative and quantitative colocalization studies of proteins at the subcellular level. Recent advances in fluorescence microscopy have made fluorescence imaging an elegant tool to study these events and image analysis has become a challenging field of study for cell biologists.

However, as images are only a representation of reality, attention must be drawn to the way in which the spatial information is collected from the sample. We have therefore pointed out basic parameters that must be tightly controlled when imaging biological samples and invite the reader to minimize perturbations that may corrupt faithful signal acquisition. This is done by the right choice of acquisition system, adapted to the size and nature of the structures to colocalize and by minimizing all forms of noise.

From our experience, automated image analysis that would be desirable for qualitative and quantitative image analysis is not an easy 'black-box' strategy. On the contrary, the full chain of events from sample preparation to image capture and analysis has to be vigorously optimized for each specimen.

To get started with colocalization analysis of any image pair, we provide the JACoP plugin, which will facilitate comparison of most of the standard analysis methods mentioned above. Having all the tools in hand, we invite the reader now to pick up the gauntlet and to walk with us on the wild side of colocalization analysis! But let's keep in mind that fluorescence microscopy is only one step towards the assessment of colocalization of two proteins, to be complemented by biochemical methods and, if possible, by electron microscopy.

Acknowledgements

We are indebted to many colleagues for helpful discussions, scientific comments, critical reading of the manuscript and constant support, including Yohann Boutté, Spencer Brown, Jim P. Dompierre and Beatrice Satiat-Jeunemaitre. We also acknowledge the ImageJ community for providing open access to a large number of plugins that we have used, prior to this collation of JACoP. This work was supported by the Association pour la Recherche contre le Cancer to the Plateforme d'Imagerie Cellulaire et Tissulaire, Institut Curie, Orsay. The Imaging and Cell Biology facility of the IFR87 (FR-W2251) 'La plante et son environnement' is supported by Action de Soutien à la Technologie et la Recherche en Essonne, Conseil de l'Essonne.

References

Abbe, E. (1873) Beiträge zur Theorie des Mikroskops und der mikroskopischen Wahrnehmung. *Schultzes Arc. F. Mikr. Anat*. **9**, 414–468.

Abbe, E. (1874) Note on the proper definition of the amplifying power of a lens or a lens system. *J. R. Microsc. Soc*. **4**, 348–351.

Bolte, S., Talbot, C., Boutte, Y., Catrice, O., Read, N.D. & Satiat-Jeunemaitre, B. (2004a) FM-dyes as experimental probes for dissecting vesicle trafficking in living plant cells. *J. Microsc*. **214**, 159–173.

Bolte, S., Brown, S. & Satiat-Jeunemaitre, B. (2004b) The N-myristoylated Rab-GTPase m-Rab$_{mc}$ is involved in post-Golgi trafficking events to the lytic vacuole in plant cells. *J. Cell Sci*. **117**, 943–954.

Bolte, S., Boutté, Y., Kluge, C., Brown, S. & Satiat-Jeunemaître, B. (2006) Tracking gene expression in plant cells: new probes for functional genomics. *Functional Plant Genomics* (ed. by J. F. Morot-Gaudry, P. Lea and J. F. Briat), Chap. Y. Science Publishers, U.K., in press.

Boutté, Y., Crosnier, M.T., Carraro, N., Traas, J. & Satiat-Jeunemaitre, B. (2006) Immunocytochemistry of the plasma membrane recycling pathway and cell polarity in plants: studies on PIN proteins. *J. Cell Sci.* **113**, 1255–1265.

Brown, S., Bolte, S. & Satiat-Jeunemaître, B. (2006) Tracking gene expression in plant cells: Microscopy and associated bio-imaging techniques. *Functional Plant Genomics* (ed. by J. F. Morot-Gaudry, P. Lea and J. F. Briat), Chap. X. Science Publishers, U.K., in press.

Castelman, K.R. (1979) *Digital Image Processing.* Prentice Hall, Englewood Cliffs.

Cordelières, F.P. (2003) *Quelle fonction pour la CLIP-170?: recherche de partenaires et nouveaux outils d'investigation*. PhD Thesis Dissertation, Université de Paris-Sud.

Costes, S.V., Daelemans, D., Cho, E.H., Dobbin, Z., Pavlakis, G. & Lockett, S. (2004) Automatic and quantitative measurement of protein-protein colocalization in live cells. *Biophys. J*. **86**, 3993–4003.

Dahan, M., Lévi, S., Luccardini, C., Rostaing, P., Riveau, B. & Triller, A. (2003) Diffusion dynamics of glycine receptors revealed by single-quantum dot tracking. *Science*, **302**, 442–445.

Demandolx, D. & Davoust, J. (1997) Multicolour analysis and local image correlation in confocal microscopy. *J. Microsc*. **185**, 21–36.

Galjart, N. (2005) CLIPs and CLASPs and cellular dynamics. *Nat. Rev. Mol. Cell Biol*. **6** (6), 487–498.

Gao, D., Knight, M.R., Trewavas, A.J., Sattelmacher, B. & Plieth, C. (2004) Self-reporting arabidopsis expressing pH and [Ca^{2+}] indicators unveil ion dynamics in the cytoplasm and in the apoplast under abiotic stress. *Plant Physiol*. **134**, 898–908.

Garini, Y., Vermolen, B.J. & Young, I.T. (2005) From micro to nano: recent advances in high-resolution microscopy. *Curr. Opin. Biotechnol*. **16**, 3–12.

Gonzales, R.C. & Woods, R.E. (1993) *Digital Image Processing*. Prentice Hall, Englewood Cliffs, New Jersey, 2nd edn 2002.

Inoué, S. (1995) *Foundations of Confocal Scanned Imaging in Light Microscopy.* Plenum Press, New York.

Jares-Erijman, E.A. & Jovin, T.M. (2003) FRET imaging. *Nat. Biotechnol.* **21**, 1387–1395.

Jaskolski, F., Mulle, C. & Manzoni, O.J. (2005) An automated method to quantify and visualize colocalized fluorescent signals. *J. Neurosci. Meth.* **146**, 42–49.

Kluge, C., Seidel, T., Bolte, S., Sharma, S., Hanitzsch, M., Satiat-Jeunemaitre, B., Ross, J., Sauer, M., Golldack, D. & Dietz, K.-J. (2004) Subcellular distribution of the V-ATPase complex in plant cells, and in vivo localisation of the 100 kDa subunit VHA-a within the complex. *BMC Cell Biol.* **5**, 29.

Lachmanovich, E., Shvartsman, D.E., Malka, Y., Botvin, C., Henis, Y.I. & Weiss, A.M. (2003) Co-localization analysis of complex formation among membrane proteins by computerized fluorescence microscopy: application to immunofluorescence co-patching studies. *J. Microsc.* **212**, 122–131.

Li, Q., Lau, A., Morris, T.J., Guo, L., Fordyce, C.B. & Stanley, E.F. (2004) A syntaxin 1, $G_{alpha}o$, and N-type calcium channel complex at a presynaptic nerve terminal: analysis by quantitative immunocolocalization. *J. Neurosci.* **24**, 4070–4081.

Manders, E.M.M. (1997) Chromatic shift in multicolour confocal microscopy. *J. Microsc.* **185**, 321–328.

Manders, E., Stap, J., Brakenhoff, G., van Driel, R. & Aten, J. (1992) Dynamics of three-dimensional replication patterns during the S-phase, analysed by double labelling of DNA and confocal microscopy. *J. Cell Sci.* **103**, 857–862.

Manders, E., Visser, A., Koppen, A., de Leeuw, W., van Liere, R., Brakenhoff, G. & van Driel, R. (2003) Four-dimensional imaging of chromatin dynamics during the assembly of the interphase nucleus. *Chromosome Res.* **11**, 537–547.

Meyer, F. & Beucher, S. (1990) Morphological segmentation. *J. Visual Comm. Image Rep.* **1** (1), 21–46.

Minsky, M. (1961) *Microscopy Apparatus*. United States Patent 3,013,467, December 19, 1961 (filed November 7, 1957).

Oppenheim, A.V., Willsky, A.S. & Young, I.T. (1983) *Signals and Systems* 2nd ed. Prentice Hall, Englewood Cliffs, New Jersey.

Pawley, J.B. (1995) *Handbook of Biological Confocal Microscopy*. Plenum Press, New York.

Rasband, W.S. (1997–2006) ImageJ. US National Institutes of Health, Bethesda, MD, U.S.A. http://rsb.info.nih.gov/ij/

Roerdink, J.B.T.M. & Meijster, A. (2000) The watershed transform: definitions, algorithms and parallelization strategies. *Fundamenta Informaticae*, **41**, 187–226.

Ronot, X. & Usson, Y. (2001) *Imaging of Nucleic Acids and Quantitation in Photonic Microscopy*. CRC Press, New York.

Scalettar, B.A., Swedlow, J.R., Sedat, J.W. & Agard, D.A. (1996) Dispersion, aberration and deconvolution in multi-wavelength fluorescence images. *J. Microsc.* **182**, 50–60.

Schuyler, S.C. & Pellman, D. (2001) Microtubule 'plus-end-tracking proteins': The end is just the beginning. *Cell*, **105** (4), 421–424.

Sibarita, J.B. (2005) Deconvolution microscopy. *Adv. Biochem. Eng. Biotechnol.* **95**, 201–243.

Sobel, I. (1970) Camera models and machine perception. PhD Thesis, Stanford University.

Tsien, R.Y. & Waggoner, A. (1995) Fluorophores for confocal microscopy. *Handbook of Biological Confocal Microscopy* (ed. by J. B. Pawley), Chap. 16. Plenum Press, New York.

Valeur, B. (2002) *Molecular Fluorescence: Principles and Applications*. Wiley-VCH, Weinheim.

Van Steensel, B., van Binnendijk, E., Hornsby, C., van der Voort, H., Krozowski, Z., de Kloet, E. & van Driel, R. (1996) Partial colocalization of glucocorticoid and mineralocorticoid receptors in discrete compartments in nuclei of rat hippocampus neurons. *J. Cell Sci.* **109**, 787–792.

Wallace, W.S.L. & Swedlow, J. (2001) A working person's guide to deconvolution in light microscopy. *Biotechniques*, **31**, 1076–1097.

Wang, Y.L. (1998) Digital deconvolution of fluorescence images for biologists. *Meth. Cell Biol.* **56**, 305–315.

Webb, R.H. & Dorey, C.K. (1995) The pixelated image. *Handbook of Biological Confocal Microscopy* (ed. by J. B. Pawley), Chap. 4. Plenum Press, New York.

Zimmermann, T., Rietdorf, J. & Pepperkok, R. (2003) Spectral imaging and its applications in live cell microscopy. *FEBS Lett.* **546**, 87–92.

Appendix

In the following, channel A and channel B grey values of voxel i will be noted as A_i and B_i, respectively, and the corresponding average intensities over the full image as a and b.

Pearson's coefficient

$$r_p = \frac{\sum_i (A_i - a) \times (B_i - b)}{\sqrt{\left[\sum_i (A_i - a)^2 \times \sum_i (B_i - b)^2\right]}}$$

Overlap coefficient

Same as previous except that the mean value is not subtracted

$$r = \frac{\sum_i A_i \times B_i}{\sqrt{\left[\sum_i (A_i)^2 \times \sum_i (B_i)^2\right]}}$$

K_1 and k_2 coefficients

$$r^2 = k_1 \times k_2 \quad \text{with} \quad k_1 = \frac{\sum_i A_i \times B_i}{\sum_i (A_i)^2} \quad \text{and} \quad k_2 = \frac{\sum_i A_i \times B_i}{\sum_i (B_i)^2}$$

M_1 and M_2 coefficient

$$M_1 = \frac{\sum_i A_{i,coloc}}{\sum_i A_i} \quad \text{and} \quad M_2 = \frac{\sum_i B_{i,coloc}}{\sum_i B_i}$$

with $A_{i,coloc}$ being A_i if $B_i > 0$ and 0 if $B_i = 0$, and $B_{i,coloc}$ being B_i if $A_i > 0$ and 0 if $A_i = 0$.

$nMDP_{xy}$ (Jaskolski et al., 2005)

$$nMDP_{xy} = \frac{(A_i - a) \times (B_i - b)}{(A_{max} - a) \times (B_{max} - b)}$$

with A_{max} being the maximum value of the A channel and B_{max} being the maximum value of the B channel.